ADVANCED MATERIALS
www.advmat.de

Potassium-Assisted Fabrication of Intrinsic Defects in Porous Carbons for Electrocatalytic CO_2 Reduction

Li-Li Ling, Long Jiao, Xiaoshuo Liu, Yun Dong, Weijie Yang, Hongjun Zhang, Bangjiao Ye, Jun Chen, and Hai-Long Jiang**

The fabrication of intrinsic carbon defects is usually tangled with doping effects, and the identification of their unique roles in catalysis remains a tough task. Herein, a K^+-assisted synthetic strategy is developed to afford porous carbon (K-defect-C) with abundant intrinsic defects and complete elimination of heteroatom via direct pyrolysis of K^+-confined metal–organic frameworks (MOFs). Positron-annihilation lifetime spectroscopy, X-ray absorption fine structure measurement, and scanning transmission electron microscopy jointly illustrate the existence of abundant 12-vacancy-type carbon defects (V_{12}) in K-defect-C. Remarkably, the K-defect-C achieves ultrahigh CO Faradaic efficiency (99%) at −0.45 V in CO_2 electroreduction, far surpassing MOF-derived carbon without K^+ etching. Theoretical calculations reveal that the V_{12} defects in K-defect-C favor CO_2 adsorption and significantly accelerate the formation of the rate-determining COOH* intermediate, thereby promoting CO_2 reduction. This work develops a novel strategy to generate intrinsic carbon defects and provides new insights into their critical role in catalysis.

1. Introduction

Porous carbon materials, featuring high surface area and excellent stability, are promising and have been intensively studied for various applications, especially in catalysis.[1] Nevertheless, given the uniform distribution of delocalized electrons, pure carbon materials are usually inert toward molecular activation, severely hindering their catalytic applications.[2] To overcome this drawback, heteroatom doping, which can induce charge delocalization, has been intensively investigated to tune the optoelectronic and chemical properties of carbon materials.[3] Almost all these studies emphasize the doping effects for enhanced performance, while the underlying influence of intrinsic carbon defects, which is usually concomitant with heteroatom doping, has been largely overlooked.[4] As a matter of fact, the carbon atoms at the edge of carbon defects, sitting in different microenvironments (abundant carbon dangling bonds) with basal-plane carbon atoms, would be greatly activated due to the unevenly distributed charge density. Therefore, to identify the role of intrinsic carbon defects and disentangle it from other influencing factors, it is imperative to fabricate defective carbons without dopants.

In fact, a few recent reports began to inspect the essential role of the intrinsic carbon defects in catalysis.[5] So far, only limited strategies, such as plasma technique, and N-dopant removal strategy, have been developed to fabricate intrinsic carbon defects.[6] Among them, the strategy of N-dopant removal, which means the formation of N-doped carbon materials followed by pyrolytic nitrogen removal at high temperatures, has been widely adopted as a facile and general route to afford precisely topological carbon defects.[5] Usually, in this method, the complete removal of N heteroatoms requires high temperatures to break C—N bonding and leave carbon defects. Unfortunately, the reconstruction of carbon network readily occurs at high temperatures, leading to the decrease of carbon defect density.[7] Given the issues described above, the fabrication of intrinsic carbon defects prefers at relatively low temperatures, making it extremely difficult to achieve the complete removal of N dopants when following N-dopant removal strategy.[7,8] To identify the activity of intrinsic carbon defects precisely, an alternative synthetic strategy to construct defective

L.-L. Ling, L. Jiao, H.-L. Jiang
Department of Chemistry
University of Science and Technology of China
Hefei, Anhui 230026, P. R. China
E-mail: jianglab@ustc.edu.cn
X. Liu, W. Yang
School of Energy and Power Engineering
North China Electric Power University
Baoding, Hebei 071003, P. R. China
X. Liu
School of Energy and Environment
Southeast University
Nanjing, Jiangsu 210096, P. R. China
Y. Dong, H. Zhang, B. Ye
State Key Laboratory of Particle Detection and Electronics
University of Science and Technology of China
Hefei, Anhui 230026, P. R. China
E-mail: hjzhang8@ustc.edu.cn
J. Chen
Intelligent Polymer Research Institute
ARC Centre of Excellence for Electromaterials Science
AIIM Facility
University of Wollongong
Innovation Campus, Wollongong, NSW 2522, Australia
The ORCID identification number(s) for the author(s) of this article can be found under https://doi.org/10.1002/adma.202205933.

DOI: 10.1002/adma.202205933

 © 2022 Wiley-VCH GmbH

Check for updates
15214095, 2022, 42, Downloaded from https://onlinelibrary.wiley.com/doi/10.1002/adma.202205933 by University Of Science, Wiley Online Library on [01/12/2022]. See the Terms and Conditions (https://onlinelibrary.wiley.com/terms-and-conditions) on Wiley Online Library for rules of use; OA articles are governed by the applicable Creative Commons License

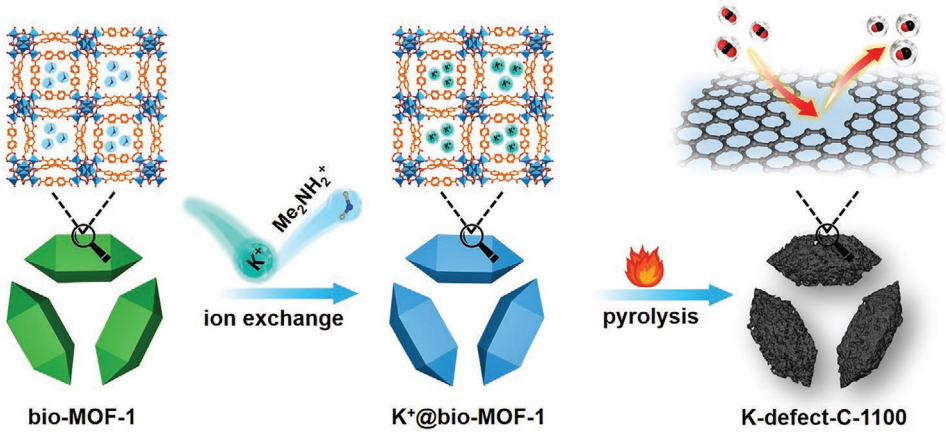

Scheme 1. Illustration for the fabrication of K-defect-C-1100 via K^+-assisted strategy. The introduction of K^+ to give K^+@bio-MOF-1 by ion exchange is crucial in the first step, prior to the pyrolysis.

carbons without doping atoms is highly desired yet remains a grand challenge. Metal–organic frameworks (MOFs),[9] a class of porous crystalline solids with exceptional porosity and structural tailorability, have been recognized as an ideal candidate to construct porous carbon-based materials.[10] Given the great advantages of structural and component regulation, MOFs might also be an ideal choice to construct intrinsic carbon defects. Unfortunately, there has never been a report on the creation of defective carbons without heteroatom dopants by the pyrolysis of MOFs.

Herein, a K^+-assisted strategy is successfully developed to create carbon defects in completely N-free carbon materials. To achieve this, an anionic MOF skeleton, bio-MOF-1 involving dimethylammonium cations ($Me_2NH_2^+$) in the 1D channels, is elaborately selected for subsequent cation exchange of $Me_2NH_2^+$ by K^+ ions, affording K^+@bio-MOF-1 (**Scheme 1**). Upon the pyrolysis of K^+@bio-MOF-1 at 1100 °C, the defect-rich porous carbon (K-defect-C-1100) with 12-vacancy-type defects (V_{12}), where 12 neighboring carbon atoms are missing, is finally obtained without N dopant, thanks to the assistance of K^+ etching. To our surprise, the resulting K-defect-C-1100 presents an ultrahigh CO Faradaic efficiency (FE) up to 99% at –0.45 V, much better than that of N-doped carbon (N-C-1100), in electrocatalytic CO_2 reduction. Theoretical calculations reveal that the V_{12} defects in K-defect-C-1100 prefer to adsorb electrophilic CO_2 molecules and significantly accelerate the formation of COOH* intermediate, accounting for its excellent performance. More importantly, as the cathode catalyst in Zn–CO_2 battery, K-defect-C-1100 also exhibits excellent CO selectivity and stability in the discharge process, illustrating the great promise of defective carbons toward energy conversion.

2. Results and Discussion

2.1. Synthesis and Structural Characterizations

The anionic bio-MOF-1, incorporating $Me_2NH_2^+$ in the pore structure to balance the negative charge on the skeleton,[11] has been synthesized (Scheme S1, Supporting Information). The involved $Me_2NH_2^+$ can be replaced with K^+ by a facile ion-exchange process,[11] yielding K^+@bio-MOF-1 with well-retained crystallinity (Figures S1 and S2, Supporting Information). The potassium content of K^+@bio-MOF-1 is determined to be 2.8 wt% by inductively coupled plasma atomic emission spectrometry (ICP-AES), revealing that ≈96% $Me_2NH_2^+$ ions are exchanged by K^+ ions in bio-MOF-1 (theoretical content of $Me_2NH_2^+$: 2.9 wt%). Thermogravimetric (TG) analysis displays a small weight loss for the parent bio-MOF-1 from 125 to 185 °C due to the loss of $Me_2NH_2^+$ (Figure S3, Supporting Information).[11] In contrast, K^+@bio-MOF-1 does not give any loss before decomposition, further indicating the replacement of $Me_2NH_2^+$ by K^+ cations (Figure S4, Supporting Information).

The pyrolysis of K^+@bio-MOF-1 and bio-MOF-1 at different temperatures gives K-defect-C-*T* and N-C-*T*, respectively (*T* represents pyrolysis temperature, *T* = 900, 1000, 1100 °C). In the pyrolysis process, the K^+ ions in K^+@bio-MOF-1 tend to react with the monodentate carboxylate on MOF skeleton and would form K_2CO_3 above ≈400 °C.[12] The generated K_2CO_3 is thermally unstable at high temperature and decomposes to K_2O species, which can further interact with N species remaining in the MOF to form small gaseous molecules containing N, such as NH_3, NO. As proved by thermogravimetry–mass spectrometry (TG–MS) analysis, the NH_3 and NO signals in the pyrolysis of K^+@bio-MOF-1 are much stronger than those of bio-MOF-1, manifesting the accelerated breakage of C—N bonds and the N removal by incorporating K^+ species (Figures S5 and S6, Supporting Information). Moreover, it can be observed that the K^+ incorporation facilitates the MOF decomposition to produce NH_3 at much lower temperature (500 °C vs 650 °C without K^+) during the pyrolysis (Figure S5, Supporting Information). These results unambiguously demonstrate that the removal of N dopant from carbon matrix is promoted and the complete N elimination thereby becomes possible at reduced temperature in the presence of K^+ species. Moreover, K_2O would react with the carbon atoms to form carbon-containing gaseous molecules (CO_2, CO, etc.) and create abundant carbon defects/vacancies (Figures S7 and S8, Supporting Information).[13] Accordingly, the K^+ species is reduced to form metallic K (boiling point: 759 °C), which readily evaporates away during pyrolysis at related temperatures. Similarly, Zn^{2+} ions are reduced to metallic Zn (boiling point: 907 °C) by the carbon and then evaporate away easily as well.

© 2022 Wiley-VCH GmbH

15214095, 2022, 42, Downloaded from https://onlinelibrary.wiley.com/doi/10.1002/adma.202205933 by University Of Science, Wiley Online Library on [01/12/2022]. See the Terms and Conditions (https://onlinelibrary.wiley.com/terms-and-conditions) on Wiley Online Library for rules of use; OA articles are governed by the applicable Creative Commons License

15214095, 2022, 42, Downloaded from https://onlinelibrary.wiley.com/doi/10.1002/adma.202205933 by University Of Science, Wiley Online Library on [01/12/2022]. See the Terms and Conditions (https://onlinelibrary.wiley.com/terms-and-conditions) on Wiley Online Library for rules of use; OA articles are governed by the applicable Creative Commons License

The powder X-ray diffraction (XRD) pattern of K-defect-C-1100 displays two broad peaks located at ≈25° and ≈44°, corresponding to the (002) and (101) crystal planes of carbon and similar results are also obtained for K-defect-C-900 and K-defect-C-1000 (Figure S9, Supporting Information). All these K-defect-C-*T* samples exhibit similar surface area and pore size distribution (Figures S10 and S11, Supporting Information). Negligible K and Zn residues can be found in K-defect-C-*T* samples based on ICP-AES data, in accordance with the X-ray photoelectron spectroscopy (XPS) analysis (Figure S12, Supporting Information). Moreover, XPS spectra also indicate that, the nitrogen signals decrease gradually with the increase of pyrolysis temperature (**Figure 1**a). When the pyrolysis temperature reaches 1100 °C, the nitrogen dopant can be totally removed in the resulting material (Figure 1a). In comparison, the direct pyrolysis of the parent bio-MOF-1 without K^+ at 1100 °C leads to the N-doped carbon material, namely, N-C-1100, in which the XPS peak of N 1s is much stronger than the K-defect-C counterparts, suggesting the obvious N residue in N-C-1100 (Figure S13, Supporting Information). The results above manifest the critical role of K^+ in promoting the removal of doped N atoms.

The content of carbon defects in K-defect-C-i has been investigated by the C 1s XPS spectra. All the C 1s spectra of K-defect-C-900, K-defect-C-1000, and K-defect-C-1100 can be fitted into three peaks corresponding to vacancy (284.1 eV), sp^2 carbon (284.5 eV), and sp^3 carbon (285.3 eV), respectively (Figure S14, Supporting Information).[14] The intensity ratio of vacancy/sp^2, which is an important parameter to evaluate the concentration of carbon defects, is further calculated. The K-defect-C-1100 possesses much higher intensity ratio of vacancy/sp^2 (0.66) than that of K-defect-C-900 (0.22) and K-defect-C-1000 (0.32), suggesting the much more abundant carbon defects in K-defect-C-1100 (Figure S15, Supporting Information). Moreover, Raman spectrum of K-defect-C-1100 shows the highest intensity ratio of D band (defect band, ≈1350 cm^{-1}) and G band (graphite band, ≈1580 cm^{-1}) (denoted as I_D/I_G) among all K-defect-C-*T* samples, indicating its highest degree of carbon disorder, in accordance with the results of C 1s XPS spectra (Figure 1b and Figure S16, Supporting Information).[15] They jointly demonstrate the successful construction of high-concentrated structural defects in K-defect-C-1100. To our surprise, the low I_D/I_G of Raman spectra for N-C-*T* samples indicating the largely reduced concentration of carbon defects for N-C-*T* compared with K-defect-C-*T* (Figures S17 and S18, Supporting Information). The above results of XPS and Raman spectra suggest that the K-defect-C-*T* possesses more carbon defects and higher disorder degree than N-C-*T* counterparts pyrolyzed at the same temperature, further demonstrating the significance of K^+ in defect construction.

2.2. Identification of the Carbon Defects in K-defect-C-1100

To obtain more details on the existing form of carbon defects, the near-edge X-ray absorption fine structure (NEXAFS)

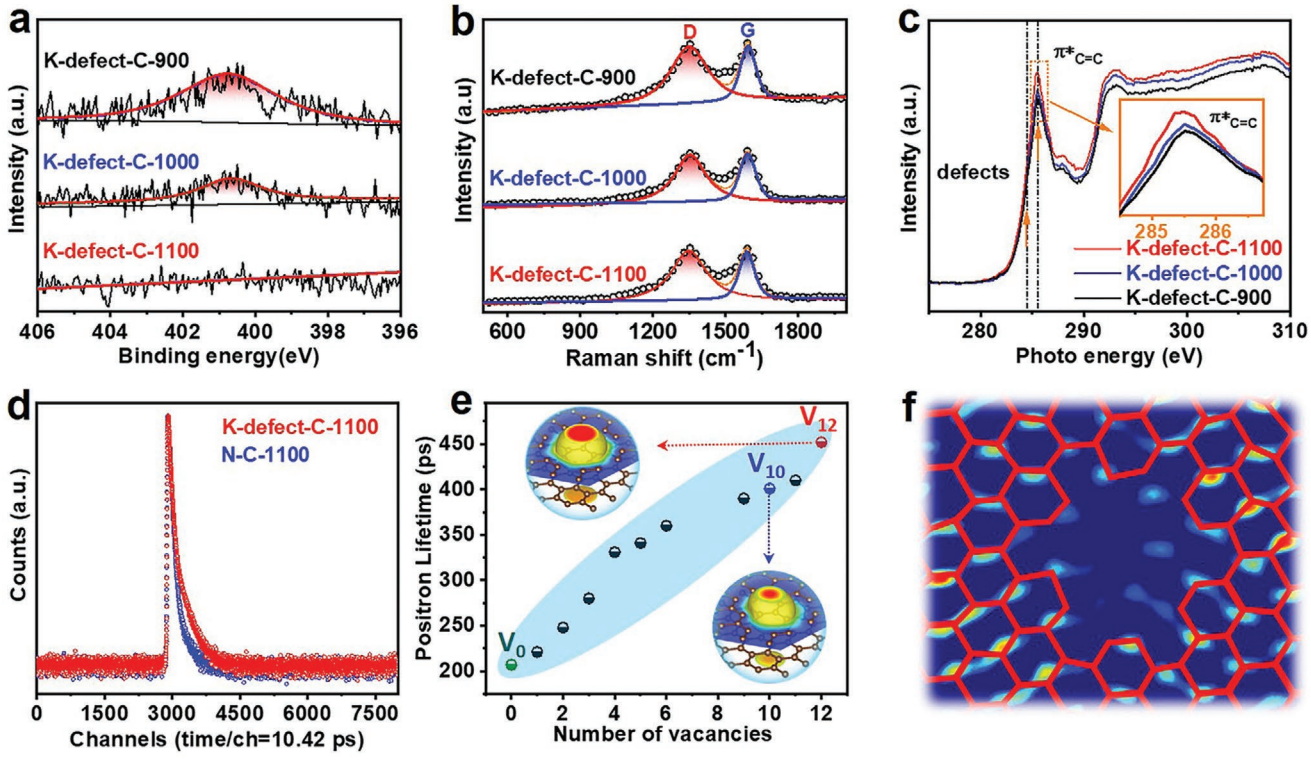

Figure 1. Structural characterizations of K-defect-C-*T* catalysts. a) N 1s XPS spectra, b) Raman spectra, and c) C K-edge NEXAFS spectra of K-defect-C-900, K-defect-C-1000, and K-defect-C-1100. d) PALS spectra of K-defect-C-1100 and N-C-1100. e) Calculated positron lifetimes of defect-free region and different vacancy-type defects with plane symmetries of vacant sites for graphite (insets: schematic representation of density distribution of positrons at V_{10} and V_{12}). f) The HAADF-STEM image of K-defect-C-1100 after fast Fourier transformation filtering.

© 2022 Wiley-VCH GmbH

measurements have been conducted. For the C K-edge NEXAFS spectra, K-defect-C-1100 presents higher absorption intensity of pre-edge adsorption (≈284.5 eV) than that of K-defect-C-1000 and K-defect-C-900, suggesting that more carbon atoms at the edge positions are created in K-defect-C-1100 (Figure 1c).[16] Moreover, the adsorption peak at 285.5 eV, which is assignable to the 1s→π^* transition of sp^2-hybridized carbon (C=C) in hexagonal graphite, shows the higher graphitization degree of K-defect-C-1100, in accordance with the aforementioned Raman analysis (Figure 1b,c and Figure S16, Supporting Information). Higher defect density and graphitization degree, as well as higher ratio of I_D/I_G in K-defect-C-1100, collectively suggest that the K^+ activation creates more and larger vacancies/holes in carbon plane (more edge carbon sites with dangling bonds) rather than localized ring defects such as intrinsic pentagonal and octagonal defects.

To gain more straightforward information on the specific size and concentration of the vacancy-type defects, positron-annihilation lifetime spectroscopy (PALS) measurements have been performed (Figure 1d).[5,17] Both PALS spectra of K-defect-C-1100 and N-C-1100 are resolved into three lifetime components (τ_1, τ_2, and τ_3, Table S1, Supporting Information). To understand the above lifetime components, density functional theory (DFT) calculations are conducted to simulate theoretical positron lifetime of various V_n defects (*n*-vacancy aggregation with plane symmetries; *n* represents the number of neighboring carbon atoms that are missing in the vacancy, Figure 1e). The shortest lifetime component (τ_1) is attributed to the positron annihilation in the defect-free region and shallow defect states, which matches with the DFT calculation results. The longest lifetime component (τ_3) corresponds to the annihilation of o-Ps (metastable bound state of a positron and an electron) in the free spaces (unoccupied space between grains). More importantly, the medium lifetime component (τ_2, 442 ps) is found for K-defect-C-1100, indicating that the positron annihilation mainly occurs at V_{12} defects (12-vacancy aggregation with plane symmetries; 12 neighboring carbon atoms are missing in the vacancy) in the graphite plane. The calculation reveals that the predominant defect type is V_{12} defects in K-defect-C-1100 (Figure 1e, inset). The τ_2 of 406 ps for N-C-1100 is close to the calculated lifetime value of V_{10} (10-vacancy aggregation with plane symmetries; 10 neighboring carbon atoms are missing in the vacancy), illustrating the existence of defects in the form of V_{10} in N-C-1100. The PALS and the above mentioned XPS results jointly demonstrate the co-existence of intrinsic defects and N doping in N-C-1100 (Figure 1e and Figure S13, Supporting Information). To gain visual evidence on the formation of V_{12} defects, high-angle annular dark-field scanning transmission electron microscopy (HAADF-STEM) observation on the K-defect-C-1100 is carried out. The STEM with the corresponding filtered image of K-defect-C-1100 nicely displays the bright spots assignable to carbon atoms and the obvious 12 neighboring carbon atoms are missing in the carbon matrix, which unambiguously manifests the successful fabrication of V_{12} defect in K-defect-C-1100 (Figure 1f). In, the above results provide solid evidence that V_{12} defects are formed with complete N removal in K-defect-C-1100 material.

2.3. Electrocatalytic Performance Evaluations for the CO_2 Reduction Reaction

Encouraged by the results above, the electrocatalytic measurements for the CO_2 reduction reaction (CO_2RR) have been then conducted. As revealed by the linear sweep voltammetry (LSV) profiles, all K-defect-C-*T* samples present more obvious current responses in CO_2 atmosphere than those in N_2 (Figures S19–S21, Supporting Information). Moreover, K-defect-C-1100 displays much larger current response than K-defect-C-900, K-defect-C-1000 as well as N-C-1100 in CO_2-saturated $KHCO_3$, indicating the higher activity of K-defect-C-1100 for CO_2 reduction (**Figure 2**a). When tested under a series of constant potentials, K-defect-C-1100 shows the highest FE of CO (FE_{CO}) up to 99% at –0.45 V, which can be largely maintained over a wide potential range from –0.35 to –0.75 V, demonstrating its ultrahigh selectivity toward CO_2 reduction compared with other counterparts (Figure 2b and Figure S22, Supporting Information). For all tested samples, CO and H_2 are the main products and no liquid product can be detected at the best potentials (Figure S23, Supporting Information). Meanwhile, K-defect-C-1100 also displays much higher CO partial current density (J_{CO}; 9.8 mA cm^{-2}@-0.85 V) than those of K-defect-C-900 (4.2 mA cm^{-2}), K-defect-C-1000 (4.6 mA cm^{-2}), and N-C-1100 (1.26 mA cm^{-2}) (Figure 2c). Moreover, K-defect-C-1100 shows larger electrochemical active surface area than K-defect-C-1000 and K-defect-C-900, further supporting the better CO_2RR performance of K-defect-C-1100 (Figure S24, Supporting Information). In addition, the best-performing K-defect-C-1100 presents ultrahigh stability with negligible current and FE_{CO} decay over a wide potential range from –0.45 to –0.65 V (Figure 2d and Figures S25 and S26, Supporting Information). All K-defect-C-*T* samples show much higher FE of CO than their N-C-*T* counterparts, indicating that the abundant carbon defects in K-defect-C-*T* samples created by K^+ greatly improve electrocatalytic performance in CO_2 reduction (Figure S27, Supporting Information). Besides, defective carbon derived from K^+@bio-MOF-1 with lower content of K^+ (1.6 wt%), named as 1.6K-defect-C-1100, shows inferior CO_2RR activity to K-defect-C-1100, further proving the significance of K^+ for the carbon defect creation and performance optimization (Figure S28, Supporting Information). The results above manifest that K-defect-C-1100 possesses the lowest potential and best FE_{CO} among all reported intrinsically defective carbon materials, and also outperforms most of metal-free carbons in electrocatalytic CO_2RR (Table S2, Supporting Information).

2.4. Performance of the Zn–CO_2 Battery

In view of the excellent electrocatalytic performance toward CO_2 reduction, K-defect-C-1100 has been further examined in a Zn–CO_2 rechargeable battery, a promising energy conversion technique for CO_2 utilization.[18] In the Zn–CO_2 battery, K-defect-C-1100 is employed as the cathode catalyst and Zn foil is used as the anode, which are then separated by a bipolar membrane to maintain different pH values in the catholyte and anolyte (**Figure 3**a and Figure S29, Supporting Information). It can be seen that, the K-defect-C-1100 cathode achieves an

© 2022 Wiley-VCH GmbH

15214095, 2022, 42, Downloaded from https://onlinelibrary.wiley.com/doi/10.1002/adma.202205933 by University Of Science, Wiley Online Library on [01/12/2022]. See the Terms and Conditions (https://onlinelibrary.wiley.com/terms-and-conditions) on Wiley Online Library for rules of use; OA articles are governed by the applicable Creative Commons License

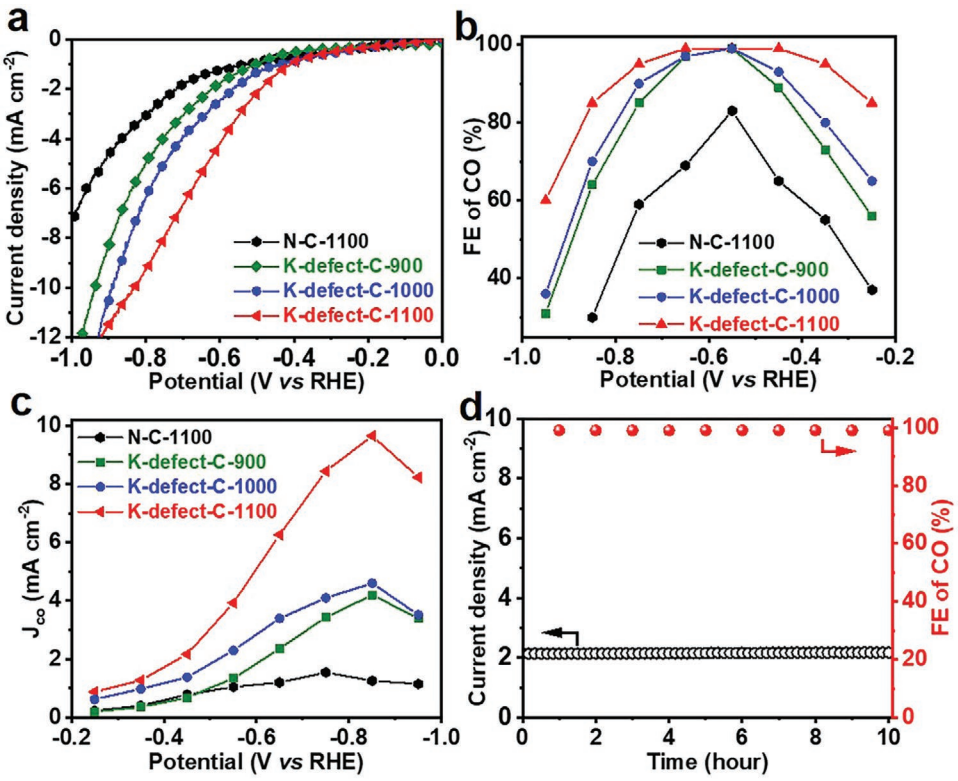

Figure 2. Electrocatalytic CO_2 reduction performances of K-defect-C-*T* catalysts. a) LSV curves, b) FEs of CO at different applied potentials, and c) the partial current densities of CO (J_{CO}) of K-defect-C-900, K-defect-C-1000, K-defect-C-1100, and N-C-1100 in CO_2-saturated 0.5 M $KHCO_3$. d) Durability test of K-defect-C-1100 at −0.45 V in 10 h.

ultrahigh FE_{CO} up to 99% in a wide discharge potential range, further suggesting its excellent CO_2 reduction performance (Figure 3b). More importantly, the Zn–CO_2 battery equipped with K-defect-C-1100 cathode catalyst demonstrates excellent discharge–charge stability during 200 cycles (Figure 3c). Overall, the very high FE_{CO} and excellent stability of K-defect-C-1100, when serving as cathode in Zn–CO_2 battery, highlight its great potential for practical applications toward the green, cost-effective, and safe utilization of CO_2.

2.5. Density Functional Theory Calculations

To acquire more insightful understanding on the reaction mechanism for CO_2RR of K-defect-C-1100, DFT calculations have been performed. Various typical carbon structural models including V_0 (defect-free in graphite), V_1 (monovacancy, 1 carbon atom is missing in the vacancy), V_{10} (10-vacancy aggregation with plane symmetries; 10 neighboring carbon atoms are missing in the vacancy), and V_{12} (12-vacancy aggregation with plane symmetries; 12 neighboring carbon atoms are missing in the vacancy) defects have been constructed (Figure S30, Supporting Information). Electrostatic potential calculations reveal that the V_{12} defect site, as the dominated defect type in K-defect-C-1100, possesses much stronger interaction with CO_2 molecules than others, giving rise to its superior ability to seize electrophilic CO_2 (Figure S31, Supporting Information). When CO_2 is further absorbed on the carbon atom around V_{12} defect site of K-defect-C-1100, the linear configuration is distorted with a bending angle of 116° (**Figure 4**a, inset). Given the COOH* formation is generally regarded as a potential rate-determining step in electrochemical CO_2 reduction,[19] the free-energy change for COOH* formation is further investigated. The free-energy change of COOH* formation on defect carbons in V_1 and V_{12} is 0.75 and 0.77 eV, much lower than that of V_0 (2.12 eV) and V_{10} (1.86 eV), implying the much higher CO_2RR activity of the catalysts involving V_{12} and V_1 sites than those with V_0 and V_{10} sites (Figure 4a, column chart). Moreover, considering the competing hydrogen evolution reaction (HER) during the CO_2RR, the energy barriers for HER and the difference between thermodynamic limiting potentials for the CO_2RR and HER (i.e., $U_L(CO_2RR) - U_L(HER)$) have also been calculated (Figure S32, Supporting Information). According to previous reports, more positive value of $U_L(CO_2RR) - U_L(HER)$ represents much higher CO_2RR selectivity.[20] It is shown that V_{12} defect sites present more positive $U_L(CO_2RR) - U_L(HER)$ value than V_0, V_1, and V_{10} sites, explaining the high CO_2RR selectivity of K-defect-C-1100 (Figure 4b).

3. Conclusions

A K^+-assisted synthetic strategy has been developed to successfully fabricate intrinsic carbon defects based on the bio-MOF-1 precursor. During the pyrolysis procedure, the K^+ ions in the MOF play an accelerating role in the removal of both N dopants

© 2022 Wiley-VCH GmbH

15214095, 2022, 42, Downloaded from https://onlinelibrary.wiley.com/doi/10.1002/adma.202205933 by University Of Science, Wiley Online Library on [01/12/2022]. See the Terms and Conditions (https://onlinelibrary.wiley.com/terms-and-conditions) on Wiley Online Library for rules of use; OA articles are governed by the applicable Creative Commons License

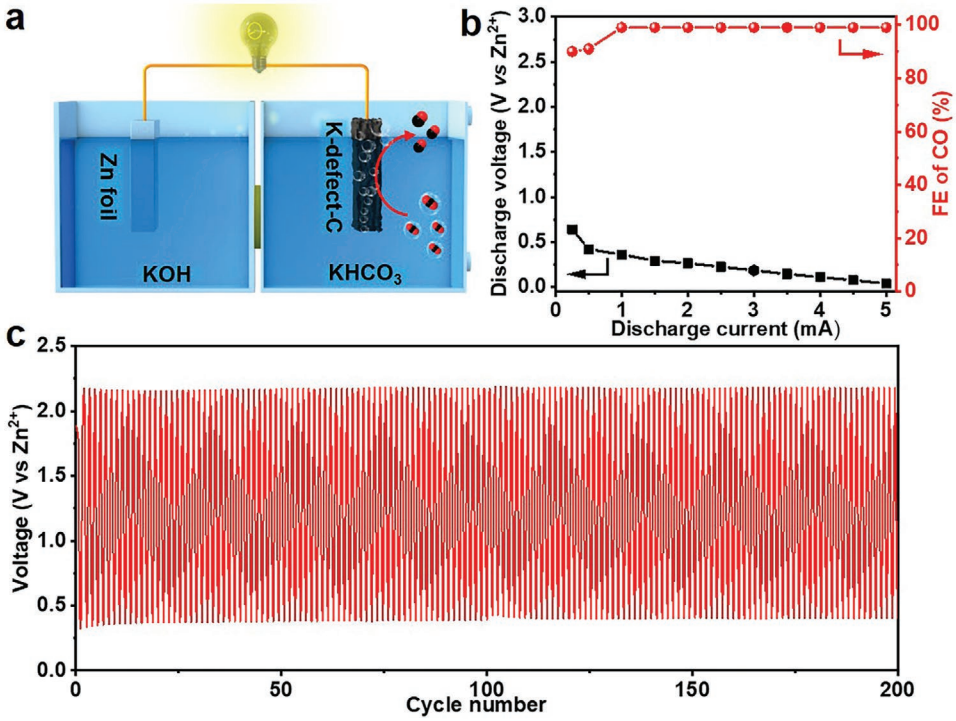

Figure 3. Zn–CO_2 battery with K-defect-C-1100 as the cathode catalyst. a) Schematic illustration of a Zn–CO_2 battery with K-defect-C-1100 as the cathode catalyst. b) Discharge voltages and the corresponding FE_{CO} profiles at different current densities. c) Galvanostatic discharge–charge cycling curves at 1.5 mA cm^{-2} for 200 cycles.

and carbon atoms in the carbon matrix, promoting the etching process and generating abundant topological defects in the carbon matrix. The K-defect-C-1100 with abundant V_{12} defects presents excellent CO_2RR activity with high CO FE up to 99% at –0.45 V, far surpassing K-defect-C-900, K-defect-C-1000, and N-C-1100 counterparts. Theoretical calculations unveil that the V_{12} defects in K-defect-C-1100 can easily seize electrophilic CO_2 molecules and greatly accelerate the formation of rate-determining COOH* intermediate, thereby promoting the CO_2RR performance. Moreover, K-defect-C-1100, as a cathode catalyst on a Zn–CO_2 battery, exhibits ultrahigh FE of CO during the discharge process with excellent stability. This work not only develops a novel synthetic strategy to create intrinsic defects in carbon materials with heteroatoms completely removed, but also provides deep insights into the understanding on carbon defects for excellent catalysis.

4. Experimental Section

Synthesis of bio-MOF-1: The bio-MOF-1 was synthesized according to the reported literature.[11] Briefly, 0.125 mmol adenine, 0.25 mmol 4,4'-biphenyl dicarboxylic acid (BPDC), 0.375 mmol $Zn(CH_3COO)_2{\cdot}2H_2O$, 1 mmol HNO_3, 13.5 mL *N*,*N*-dimethylformamide (DMF), and 1 mL H_2O were added to a 20 mL vial and heated at 130 °C for 24 h. Then the mixture was centrifuged and washed with DMF and ethanol for three times. Finally, the white solid was dried at 60 °C under vacuum to afford bio-MOF-1.

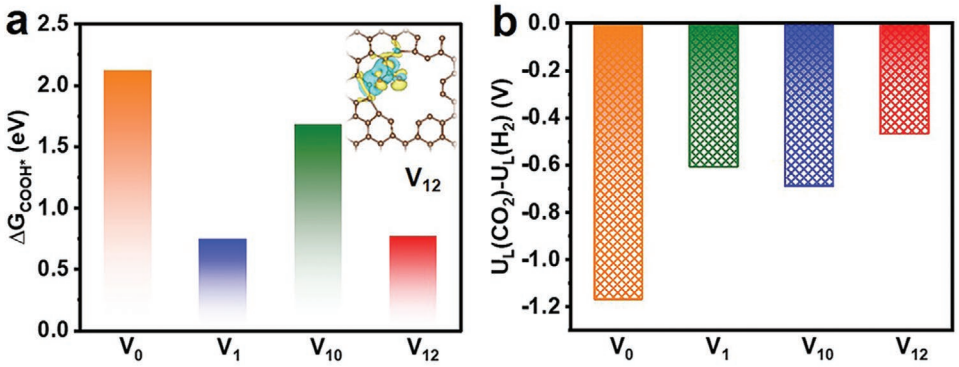

Figure 4. Density functional theory calculations. a) Free energy changes of COOH* formation (inset: electron density difference analysis of CO_2 adsorbed on V_{12}, yellow and cyan stand for charge accumulation and depletion, respectively) and b) the values of $U_L(CO_2RR) - U_L(HER)$ on V_0, V_1, V_{10}, and V_{12} sites.

© 2022 Wiley-VCH GmbH

15214095, 2022, 42, Downloaded from https://onlinelibrary.wiley.com/doi/10.1002/adma.202205933 by University Of Science, Wiley Online Library on [01/12/2022]. See the Terms and Conditions (https://onlinelibrary.wiley.com/terms-and-conditions) on Wiley Online Library for rules of use; OA articles are governed by the applicable Creative Commons License

Synthesis of K⁺@bio-MOF-1: The K⁺@bio-MOF-1 was synthesized via a K^+ ion-exchange process. Typically, 150 mg bio-MOF-1 was dispersed in a saturated solution of KCl in DMF. Then, the mixture was magnetically stirred for 2 h and then centrifuged to remove the solution. The obtained white solid was re-dispersed into a saturated DMF solution of KCl and the ion-exchange process was repeated twice with the stirring time of 2 and 24 h, respectively. After the cation-exchange process, the solid was collected by centrifugation and rinsed in DMF and acetone, finally dried at 60 °C under vacuum to yield K⁺@bio-MOF-1. The K⁺@bio-MOF-1 with low content of K^+ (1.6 wt%), named as 1.6K⁺@bio-MOF-1, was also prepared using a solution of KCl in DMF (10×10^{-3} M), and other parameters are almost the same as K⁺@bio-MOF-1.

Synthesis of K-Defect-C-T and N-C-T (T Represents the Pyrolysis Temperature): To obtain the defective carbon, the as-synthesized K⁺@bio-MOF-1 was heated at 900, 1000, or 1100 °C in a heating rate of 5 °C min^{-1} for 2 h in N_2 flow, followed by slowly cooling down to room temperature. The obtained carbon materials were washed with HCl (1 M) for 4 h to remove the inorganic impurity and the K-defect-C-*T* (*T* represents the pyrolysis temperature) materials were finally obtained. The 1.6K-defect-C-1100 was obtained by pyrolysis of 1.6K⁺@bio-MOF-1 at 1100 °C. The N-C-*T* (*T* represents the pyrolysis temperature) was synthesized by replacing K⁺@bio-MOF-1 with the parent bio-MOF-1, while other parameters were almost the same as those for K-defect-C-*T*.

Supporting Information

Supporting Information is available from the Wiley Online Library or from the author.

Acknowledgements

L.L., L.J., and X.L. contributed equally to this work. This work was supported by the National Key Research and Development Program of China (2021YFA1500400), the National Natural Science Foundation of China (21725101, 22161142001, 22001242, and 11975225), and the Fundamental Research Funds for the Central Universities (WK2060000040, WK2060000038).

Conflict of Interest

The authors declare no conflict of interest.

Data Availability Statement

The data that support the findings of this study are available from the corresponding author upon reasonable request.

Keywords

CO_2 conversion, defects, electrocatalysis, metal–organic frameworks, porous carbon

Received: June 29, 2022
Revised: July 24, 2022
Published online: September 16, 2022

[1] a) C. Hu, R. Paul, Q. Dai, L. Dai, *Chem. Soc. Rev.* **2021**, *50*, 11785; b) J. Liang, Y. Jiao, M. Jaroniec, S. Z. Qiao, *Angew. Chem., Int. Ed.* **2012**, *51*, 11496; c) S. Zhao, D.-W. Wang, R. Amal, L. Dai, *Adv. Mater.* **2019**, *31*, 1801526.

[2] a) L. Dai, Y. Xue, L. Qu, H. Choi, J. Baek, *Chem. Rev.* **2015**, *115*, 4823; b) C. Su, M. Acik, K. Takai, J. Lu, S. Hao, Y. Zheng, P. Wu, Q. Bao, T. Enoki, Y. J. Chabal, K. P. Loh, *Nat. Commun.* **2012**, *3*, 1298.

[3] a) H. Wang, Y. Shao, S. Mei, Y. Lu, M. Zhang, J. Sun, K. Matyjaszewski, M. Antonietti, J. Yuan, *Chem. Rev.* **2020**, *120*, 9363; b) K. Gong, F. Du, Z. Xia, M. Durstock, L. Dai, *Science* **2009**, *323*, 760; c) T. Y. Ma, S. Dai, M. Jaroniec, S. Z. Qiao, *Angew. Chem., Int. Ed.* **2014**, *53*, 7409.

[4] a) J. Lahiri, Y. Lin, P. Bozkurt, I. I. Oleynik, M. Batzill, *Nat. Nanotechnol.* **2010**, *5*, 326; b) X. Yan, Y. Jia, X. Yao, *Chem. Soc. Rev.* **2018**, *47*, 7628; c) F. Banhart, J. Kotakoski, A. V. Krasheninnikov, *ACS Nano* **2011**, *5*, 26.

[5] a) Y. Jiang, L. Yang, T. Sun, J. Zhao, Z. Lyu, O. Zhuo, X. Wang, Q. Wu, J. Ma, Z. Hu, *ACS Catal.* **2015**, *5*, 6707; b) L. Tao, M. Qiao, R. Jin, Y. Li, Z. Xiao, Y. Wang, N. Zhang, C. Xie, Q. He, D. Jiang, G. Yu, Y. Li, S. Wang, *Angew. Chem., Int. Ed.* **2019**, *58*, 1031; c) Y. Jia, L. Zhang, L. Zhuang, H. Liu, X. Yan, X. Wang, J. Liu, J. Wang, Y. Zheng, Z. Xiao, E. Taran, J. Chen, D. Yang, Z. Zhu, S. Wang, L. Dai, X. Yao, *Nat. Catal.* **2019**, *2*, 688.

[6] a) S. Chen, J. Bi, Y. Zhao, L. Yang, C. Zhang, Y. Ma, Q. Wu, X. Wang, Z. Hu, *Adv. Mater.* **2012**, *24*, 5593; b) S. Dou, L. Tao, R. Wang, S. El Hankari, R. Chen, S. Wang, *Adv. Mater.* **2018**, *30*, 1705850; c) Y. Jia, L. Zhang, A. Du, G. Gao, J. Chen, X. Yan, C. L. Brown, X. Yao, *Adv. Mater.* **2016**, *28*, 9532.

[7] a) V. Mazánek, J. Luxa, S. Matějková, J. Kučera, D. Sedmidubský, M. Pumera, Z. Sofer, *ACS Nano* **2019**, *13*, 1574; b) Y. Dong, Q. Zhang, Z. Tian, B. Li, W. Yan, S. Wang, K. Jiang, J. Su, C. W. Oloman, E. L. Gyenge, R. Ge, Z. Lu, X. Ji, L. Chen, *Adv. Mater.* **2020**, *32*, 2001300.

[8] W. Wang, L. Shang, G. Chang, C. Yan, R. Shi, Y. Zhao, G. I. N. Waterhouse, D. Yang, T. Zhang, *Adv. Mater.* **2019**, *31*, 1808276.

[9] a) H. Furukawa, K. E. Cordova, M. O. Keeffe, O. M. Yaghi, *Science* **2013**, *341*, 1230444; b) M. Ding, R. W. Flaig, H.-L. Jiang, O. M. Yaghi, *Chem. Soc. Rev.* **2019**, *48*, 2783; c) T. Islamoglu, S. Goswami, Z. Li, A. J. Howarth, O. K. Farha, J. T. Hupp, *Acc. Chem. Res.* **2017**, *50*, 805; d) B. Li, H. Wen, Y. Cui, W. Zhou, G. Qian, B. Chen, *Adv. Mater.* **2016**, *28*, 8819; e) L. Jiao, Y. Wang, H.-L. Jiang, Q. Xu, *Adv. Mater.* **2018**, *30*, 1703663; f) D. Liu, J. Wan, G. Pang, Z. Tang, *Adv. Mater.* **2018**, *31*, 1803291; g) X. Zhao, Y. Wang, D. S. Li, X. Bu, P. Feng, *Adv. Mater.* **2018**, *30*, 1705189.

[10] a) B. Liu, H. Shioyama, T. Akita, Q. Xu, *J. Am. Chem. Soc.* **2008**, *130*, 5390; b) Y. Kaneti, J. Tang, R. R. Salunkhe, X. Jiang, A. Yu, K. C.-W. Wu, Y. Yamauchi, *Adv. Mater.* **2017**, *29*, 1604898; c) K. J. Lee, J. H. Lee, S. Jeoung, H. R. Moon, *Acc. Chem. Res.* **2017**, *50*, 2684; d) Y.-Z. Chen, R. Zhang, L. Jiao, H.-L. Jiang, *Coord. Chem. Rev.* **2018**, *362*, 1; e) Z. Liang, T. Qiu, S. Gao, R. Zhong, R. Zou, *Adv. Energy Mater.* **2022**, *12*, 2003410.

[11] a) J. An, S. J. Geib, N. L. Rosi, *J. Am. Chem. Soc.* **2009**, *131*, 8376; b) J. An, N. L. Rosi, *J. Am. Chem. Soc.* **2010**, *132*, 5578.

[12] a) Y. Jiang, Z. Jiang, M. Shi, L. Zheng, S. Liang, J. Feng, R. Sheng, S. Zhang, T. Wei, Z. Fan, *Carbon* **2021**, *182*, 559; b) B. Liu, R. Shi, X. Ma, R. Chen, K. Zhou, X. Xu, P. Sheng, Z. Zeng, L. Li, *Carbon* **2021**, *181*, 270; c) M. Sevilla, A. B. Fuertes, *ACS Nano* **2014**, *8*, 5069.

[13] a) Z. Yang, Y. Wang, Z. Dai, Z. Lu, X. Gu, H. Zhao, G. Sun, W. Lan, Z. Zhang, X. Pan, J. Zhou, E. Xie, *Carbon* **2019**, *146*, 610; b) J. Wang, S. Kaskel, *J. Mater. Chem.* **2012**, *22*, 23710.

[14] J. Lee, R. Kim, S. Kim, J. Heo, H. Kwon, J. H. Yang, H. Kim, *Energy Environ. Sci.* **2020**, *13*, 2839.

[15] H. Zhang, Y. Liu, T. Chen, J. Zhang, J. Zhang, X. W. D. Lou, *Adv. Mater.* **2019**, *31*, 1904548.

[16] a) C. Zhao, Y. Wang, Z. Li, W. Chen, Q. Xu, D. He, D. Xi, Q. Zhang, T. Yuan, Y. Qu, J. Yang, F. Zhou, Z. Yang, X. Wang, J. Wang, J. Luo, Y. Li, H. Duan, Y. Wu, Y. Li, *Joule* **2019**, *3*, 584; b) Y. Zheng, Y. Jiao, Y. Zhu, L. H. Li, Y. Han, Y. Chen, A. Du, M. Jaroniec, S. Z. Qiao, *Nat. Commun.* **2014**, *5*, 3783.

© 2022 Wiley-VCH GmbH

15214095, 2022, 42, Downloaded from https://onlinelibrary.wiley.com/doi/10.1002/adma.202205933 by University Of Science, Wiley Online Library on [01/12/2022]. See the Terms and Conditions (https://onlinelibrary.wiley.com/terms-and-conditions) on Wiley Online Library for rules of use; OA articles are governed by the applicable Creative Commons License

[17] Z. Tang, M. Hasegawa, T. Shimamura, Y. Nagai, T. Chiba, Y. Kawazoe, M. Takenaka, E. Kuramoto, T. Iwata, *Phys. Rev. Lett.* **1999**, *82*, 2532.
[18] J. Xie, Y. Wang, *Acc. Chem. Res.* **2019**, *52*, 1721.
[19] a) W. Ren, X. Tan, W. Yang, C. Jia, S. Xu, K. Wang, S. C. Smith, C. Zhao, *Angew. Chem., Int. Ed.* **2019**, *58*, 6972; b) L. Jiao, J. Zhu, Y. Zhang, W. Yang, S. Zhou, A. Li, C. Xie, X. Zheng, W. Zhou, S.-H. Yu, H.-L. Jiang, *J. Am. Chem. Soc.* **2021**, *143*, 19417; c) Z. Wu, H. Wu, W. Cai, Z. Wen, B. Jia, L. Wang, W. Jin, T. Ma, *Angew. Chem., Int. Ed.* **2021**, *60*, 12662.
[20] a) L. Jiao, W. Yang, G. Wan, R. Zhang, X. Zheng, H. Zhou, S.-H. Yu, H.-L. Jiang, *Angew. Chem., Int. Ed.* **2020**, *59*, 20589; b) D. Kim, C. Xie, N. Becknell, Y. Yu, M. Karamad, K. Chan, E. J. Crumlin, J. K. Nørskov, P. Yang, *J. Am. Chem. Soc.* **2017**, *139*, 8329.

© 2022 Wiley-VCH GmbH

15214095, 2022, 42, Downloaded from https://onlinelibrary.wiley.com/doi/10.1002/adma.202205933 by University Of Science, Wiley Online Library on [01/12/2022]. See the Terms and Conditions (https://onlinelibrary.wiley.com/terms-and-conditions) on Wiley Online Library for rules of use; OA articles are governed by the applicable Creative Commons License